Nanoimmunosensor based on ZnO nanorods for ultrasensitive detection of 17β-Estradiol

Aruna Chandra Singh[a], M.H. Asif[d,1], Gautam Bacher[c], Bengt Danielsson[d], Magnus Willander[b,*], Sunil Bhand[a,*]

[a] *Biosensor Lab, Department of Chemistry, BITS, Pilani-K.K. Birla Goa Campus, Goa 403726, India*
[b] *Physical Electronics and Nanotechnology Division, Department of Science and Technology (ITN) Campus Norrköping, Linköping University, Norrköping SE-60174, Sweden*
[c] *Department of EEE, BITS, Pilani-K.K. Birla Goa Campus, Goa 403726, India*
[d] *Acromed Invest AB, Magistratsvägen 10, SE 226 43 Lund, Sweden*

ARTICLE INFO

ABSTRACT

Advances in nanostructured materials have facilitated the development of novel sensitive techniques for detection of environmental and clinical analytes. There is immense need for development of devices that can detect analytes at concentrations as low as few pg mL^{-1}. The comparable size of nanostructured materials and biomolecules enabled the integration of biological systems with nanometer sized structures. Herein, we demonstrate a Zinc Oxide nanorods (ZnONRs) integrated ultrasensitive label-free biosensor with femtomolar (0.01 pg mL^{-1}) sensitivity for the endocrine disruptor 17β-Estradiol (E2). The ZnONRs, average width 50 nm and length 325 nm, were grown on the silver electrode surface (Ag-ZnONRs). Monoclonal antibodies of E2 (mAb-E2) were covalently immobilized on ZnONRs surface and measured using electrochemical impedance spectroscopy (EIS). A linear detection range of 0.1–200 pg mL^{-1} for E2 with R^2 = 0.99 and % RSD = 4.35 (n = 3, assay volume 90 μL) was achieved for the developed nano-sensing system. A significant enhancement in the sensitivity was achieved in the presence of ZnONRs, enabling the limit of quantification down to 0.1 pg mL^{-1} with 2.7 % capacitance change per decade. In addition, a further increase in sensitivity due to assay volume reduction (20 μL) was observed enabling further scope of miniaturization.

1. Introduction

Recent literature reports the involvement of nanostructures in biological and chemical systems with novel applications in a new generation of miniaturized, smart biosensing devices (Soleymani et al., 2009). The performance of a nanostructure-based biosensor can be improved by tailoring the properties of the metal oxide–biomolecules interface through engineering of morphology, effective surface area, functionality, adsorption capability and electron-transfer properties. These interactions of nanostructures with biomolecules have opened a wide range of applications (Wang, 2005; Zhu et al., 2015). Due to their unique properties such as high surface to volume ratio, surface-catalytic activities, immobilization of biomolecules, labeling biomolecules, catalysis of electrochemical reactions and enhancement of electron transfer, they have gained special attention in development of analytical platforms (Luo et al., 2006; Pal and Bhand, 2015). Based on their

various applications in design and development of electrochemical sensor systems, these nanostructures are subject of considerable research and can be integrated with various functional nanodevices (Perumal et al., 2015). In the last decade, various nanostructures of zinc oxide, gold and titanium dioxide have already been reported as major potential candidates in biosensing applications (Bülbül et al., 2015).

Zinc oxide (ZnO), a polar semiconducting material with high catalytic efficiency, biocompatibility, chemical stability in physiological environments, low toxicity and a high isoelectric point (IEP) of about 9.5, has found abundant use in biosensing applications (Soomro et al., 2012). ZnO nanostructures (ZnONSs) with various shapes such as nanorods, nanowalls and nanobelts have been reported in fabrication of biosensors for the detection of biomarkers (Yue et al., 2014). Due to the high electrochemical stability, ZnO can be doped easily and economically compared to other semiconducting nanostructures. ZnO is an important multifunctional material with wide applications in chemical,

biochemical sensors and optical devices. In recent years, ZnONSs have gained significant potential for biosensing applications because of its unique features such as small dimensions, increased sensing surface and strong binding properties. ZnONSs show great promise for faster response and higher sensitivity than planar sensor configurations (Asif et al., 2009, 2010a). Interestingly, ZnONSs grown on various substrates including glass, silicon and conductive surfaces like Indium-tin-oxide (ITO), copper and gold have been reported with different morphologies (Ahmad, and Yakimova et al., 2009, 2012). A myriad of ZnONSs such as wires, nanorods, fibers, flowers and nanocomposite synthesized from various physical and chemical routes have been reported for biosensing applications (Willander et al., 2008; Ahmad et al., 2010; Xia et al., 2010; Sonnenschein and Soto, 1998). ZnONRs based optical biosensor have been reported for detection of Choline and Ochratoxin A (Pal and Bhand, 2015 and Viter et al., 2018). While the ZnONSs have been mainly reported for glucose, bacteria and neurotransmitter detection, there are no such reports for ultrasensitive detection of Endocrine disrupting chemicals (EDCs) using ZnONRs. In the present work, ZnONRs coupled electrodes were deployed for the development of ultrasensitive impedimetric biosensors. The effect of ZnONRs structure on the sensitivity and volume reduction was investigated for detection of 17β-Estradiol (E2).

The increasing burden of global water problems demands an urgent need for ultrasensitive and affordable analytical devices. EDCs constitute a wide group of environmental pollutants and mainly found in the man-made materials such as steroids, pesticides, metals, additives or contaminants in food and personal care products (Nohynek et al., 2013). According to the European Union (EU), EDCs are defined as "an exogenous substance that causes adverse health effects in an intact organism, or its progeny, secondary to changes in endocrine function" (Zoeller et al., 2012). The World Health Organization (WHO) and United Nations Environment Programme (UNEP) have identified three distinct sets of health endpoints with the most substantial evidence for EDC attribution namely obesity/diabetes, male reproductive health, and neurodevelopment disability (Damstra et al., 2002). The quantification of E2 in environment from the excreta of human and animal, i.e. urine and faeces is important in various clinical evaluations including human fertility, gynaecomastia (Rosner et al., 2013), hyperandrogenism, rise in the probability of cancer and reduction in the proportion of male births (Le et al., 2017). Various international agencies have put stringent limits for presence of E2 in water. EU has fixed a range 0.4–0.9 ng kg^{-1} and Codex Alimentarius Commission (CAC) 0–0.05 µg kg^{-1} (Codex Alimentarius Commission, 2012). Hence, the need for development of an ultrasensitive, easy to use biosensor for low level detection of EDCs is of immense interest.

In the present work, ZnONRs have been grown on Ag electrode surface by low temperature aqueous chemical process (Asif et al., 2010b). The average size of the ZnONRs was found to be 50 nm wide and 325 nm long as observed under scanning electron microscopy (SEM) of individual array and used further for immunosensor development. The immunosensor was fabricated on Ag-ZnONRs modified electrode coupled with mAb-E2 using self-assembled monolayers (SAMs) of 16-Phosphohexaundecanoic acid (16-PHA) (Ag-ZnONRs-16-PHA-mAb-E2), as shown in Scheme 1. A miniaturized dual electrode set-up was used for measurement of change in electrochemical signals during antigen-antibody interaction using EIS. The physical dimensions, biocompatibility, short analysis time, high sensitivity and ease of use for the constructed sensor enabled excellent limit of detection (LOD:0.01 pg mL^{-1}) with a linear range of 0.1–200 pg mL^{-1}. The results thus obtained showed significant enhancement in the sensitivity enabling detection of down to 10 femtogram of E2 in 90 µL assay volume.

2. Materials and methods

2.1. Materials and reagents

All the chemicals used were of analytical grade and were used as received. Anti-17β-estradiol antiserum, primary monoclonal antibody (mAb) raised in mouse was procured from AbCam, UK. The chemicals; 17β-estradiol, 16-phosphonohexadecanoic acid (16-PHA), 1-ethyl-3-[3-dimethylaminopropyl] carbodiimide hydrochloride (EDC), and N-hydroxy succinimide (NHS) were purchased from Sigma–Aldrich, USA. Absolute ethanol, 100% was purchased from TEDIA, USA. Hydrogen peroxide (H_2O_2) 30% (w/v), di-sodium hydrogen phosphate (Na_2HPO_4), sodium di-hydrogen phosphate (NaH_2PO_4) from MERCK (Germany). For sample handling, electronic micropipettes (eppendorf®, Germany) were used. Shaking of the samples was done by Spinix shaker (Tarsons, India). For preparing all the solutions, water produced in a Milli-Q system (Millipore, Bedford, MA, USA) was used. Eular grade certified ultrahigh pure nitrogen (99.9%), pH meter (Seven Multi Mettler Toledo, 8603, Switzerland) and NUNC 384 polystyrene well plate (obtained through Sigma Aldrich, USA, capacity 120 µL per well) were used.

2.2. Instrumentation

2.2.1. Surface characterization tools

Fourier Transform InfraRed (FT-IR) spectra were recorded using IRAffinity-1 (SHIMADZU, Japan) with attenuated total reflectance (ATR) attachment Specac Diamond ATR AQUA. For the ZnONR samples, FT-IR ATR spectra were collected with data resolution of 4 cm^{-1} (64 scans). The binding of mAb-E2 to the electrode surface was confirmed by using an inverted fluorescence microscope IX71 (Olympus, Japan) attached to a charged coupled device camera (CCD), ORCA ERII (Hamamatsu Photonic, UK). The surface morphology of bare and modified electrodes was studied using Field Emission Scanning Electron Microscope (FE-SEM), FEI Quanta 250 FEG for Ag-ZnONRs and for mAb Carl Zeiss, Neon 40 Crossbeam, Germany. Elemental analysis was carried out using Energy Dispersive X-ray (EDX) spectrometer, EDAX Inc. USA. Atomic Force Microscopy (AFM)) studies were carried out using NTEGRA Prima (NT-MDT, Russia).

2.2.2. EIS measurements

EIS measurements were performed on IVIUM CompactStat impedance analyzer (The Netherlands). The response of Ag-ZnONR nanoimmunosensor was recorded by immersing the sensor in 90 µL PBS (10 mM, pH 7.4). The EIS spectra of the real and imaginary parts of impedance, Z′ and Z″ were recorded in the frequency range 1–100 kHz with an applied AC potential of 10 mV. For stability and sustainability of the design of the developed immunosensor, all measurements were recorded at room temperature. The sensitivity of the Ag-ZnONR-coupled sensor was evaluated as a function of capacitance change.

2.3. Growth of ZnONRs on silver wire surface

ZnONRs were grown on the silver (Ag) wire surface using an aqueous chemical growth (ACG) technique (Asif et al., 2010b). Equimolar concentrations of zinc nitrate hexahydrate [Zn (NO$_3$)$_2$·6H$_2$O, 99.9% purity] and hexamethylenetetramine ($C_6H_{12}N_4$, 99.9% purity) solutions were used for growth of ZnONRs on the Ag wire. The Ag wire substrates were immersed into the solution and tilted against the wall of the beaker that was put into an oven at low temperature for different times to get aligned ZnO nanostructure (Xia et al., 2010). Structural morphology and size distribution of the Ag-ZnONRs were investigated by FEG-SEM at different magnifications. The ZnONRs cover about a half part of the Ag wire. The nanostructure has a rod like shape with a hexagonal cross section and primarily aligned along the perpendicular direction. The nanorods were uniform in size with an average diameter
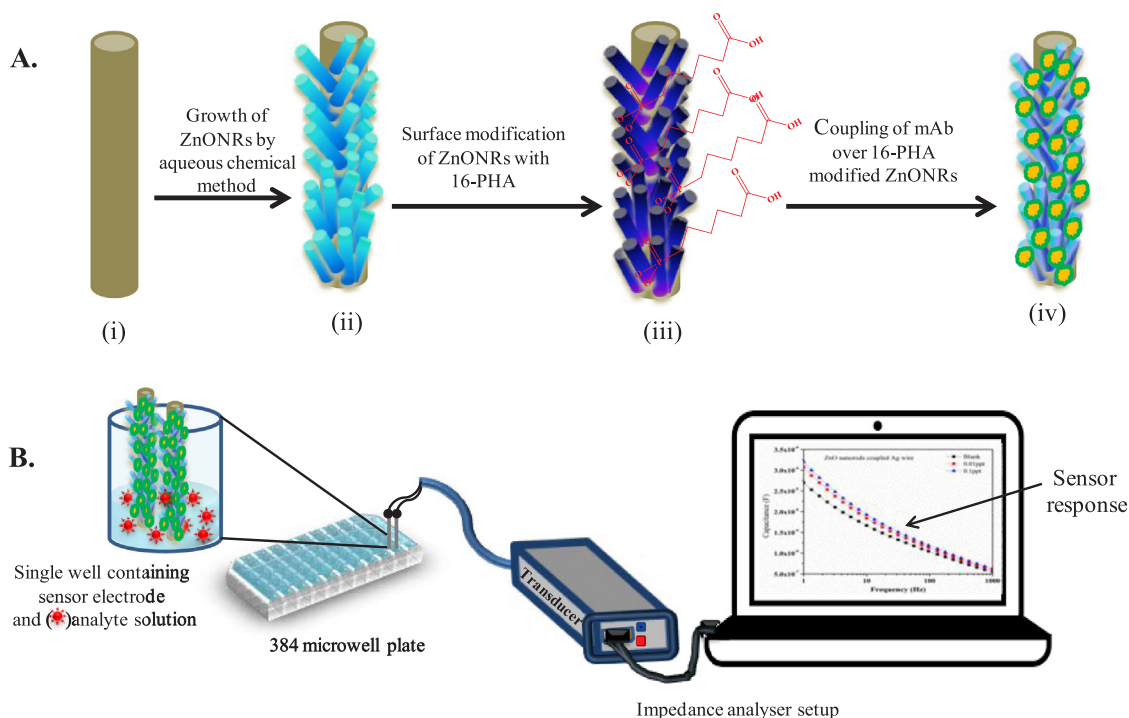
Scheme 1. Schematic representation of nanoimmunosensor construction; **A.** Preparation of ZnONRs-E2 probe **(i)** Ag wire electrode **(ii)** ZnONRs grown on Ag wire electrode **(iii)** Self assembly of 16-PHA on Ag-ZnONRs **(iv)** mAb-E2 functionalized Ag-ZnONRs **B.** EIS measurement setup comprising a pair of Ag-ZnONRs-mAb-E2 in 384 well format connected via impedance analyzer.

of 50 nm.

2.4. ZnONRs-coupled sensing electrodes

The selected Ag-ZnONRs wire electrodes were cleaned with deionized water for removing inorganic surface impurities and dried under pure nitrogen stream. Subsequently, they were rinsed with ethanol and dried under nitrogen. In order to prepare self-assembled monolayers, these wires were submerged into the 0.5 mM solution of freshly prepared 16-PHA in absolute ethanol for 72 h. The electrodes were again rinsed with absolute ethanol followed by rinsing with distilled water and allowed to dry under a nitrogen stream. Unreacted terminal carboxylic groups were passivated with an aqueous equimolar solution (100 mM) EDC/NHS under vacuum environment for mAb-E2 immobilization. The resultant NHS ester monolayers were incubated for 12 h in a solution of mAb-E2 (1:1000; 2.4×10^{-3} mg mL^{-1}) followed by washing with the phosphate buffer.

3. Results and discussion

3.1. Surface characterization

3.1.1. Fourier Transform Infrared spectroscopy (FT-IR)

Surface modifiers are often acidic and may alter the surface chemistry or etch the oxide which is usually observed with modifiers such as thiol, carboxyl, and phosphonate linkers (Bulusu et al., 2013). Additionally, careful choice of solvent and deposition condition for SAMs can reduce the degree of material etching. Functionalization of ZnONRs is most frequently carried out using organic species containing carboxylic groups (–COOH) which bind to the oxide surface through the deprotonated species (Hsuan and Andrew, 2015). The coupling of 16-PHA on the Ag-ZnONR electrode via phosphonation and subsequent coupling of mAb-E2 were studied using ATR-FT-IR spectroscopy, since carboxyl linkages tend to be more stable under wet conditions than –NH$_2$ and –OH bonds. FT-IR spectrum of bare, phosphonated and mAb-E2 coupled Ag-ZnONRs have been studied and presented in Fig. 1A. The

characteristic vibrational bands of asymmetric (ν_{as}, C-H) and symmetric (ν_s, C-H) stretching of methylene group of 16-PHA were observed at 2918 cm^{-1} and 2855 cm^{-1} on phosphonated Ag-ZnONRs (Fig. 1A (ii)). The presence of vibrational bands corresponds to methylene group suggesting the formation of self-assembled monolayers of 16-PHA on the Ag-ZnONRs. Presence of C=O stretching (ν_s) at 1710 cm^{-1} on Ag-ZnONR is characteristic of an organic carboxylic compound. Additionally, the presence of vibrational bands at 1462 cm^{-1}, 1414 cm^{-1} and 1231 cm^{-1} can be ascribed to C–H deformation and C–O stretch, respectively. In the P–O stretching region, the binding mode in formation of phosphonic acid onto metal oxides is not easy to elucidate. The peaks correspond to the P–O stretching region appear between 1303 cm^{-1} and 784 cm^{-1} and the presence of several different binding modes in phosphonic acid monolayers is indicated by the presence of residual P = O and P–O–H sites. The peak that appeared at 944 cm^{-1} was assigned to a P–OH band that is observed only after binding to the Ag-ZnONRs surface. This indicates that the phosphonic acid has successfully bound to the ZnO surface via covalent coupling. The chemical bonding to the ZnONR surface is only possible through monodentate ester linkages, which leave the carbonyl group unaffected by the bonding; bidentate chelation to a single Zn center through both oxygen atoms and bidentate bridging between both oxygen atoms and two Zn centers (Cornil et al., 2014). The existence of the peak at 1079 cm^{-1}, which is characteristic of the P = O stretching mode strongly suggested the evidence for bidentate binding modes. The observation of P–OH related modes indicates that the binding of 16-PHA on ZnONR occurs mainly through the PO$_3$H$_2$ groups. Similarly, coordination of binding modes of organic phosphonic acids on ZnO was also confirmed. The mAb-E2 coupling through 16-PHA SAMs via the carbodiimide cross-linking reaction on Ag-ZnONRs surfaces is depicted in Fig. 1A (iii). The appearance of three new vibrational bands at 1646 cm^{-1}, 1566 cm^{-1} and 1247 cm^{-} after immobilization of mAb-E2[1] can be ascribed to the formation of amide bonds between mAb-E2 and the 16-PHA functionalized to Ag-ZnONRs (Fig. 1A (iii)).
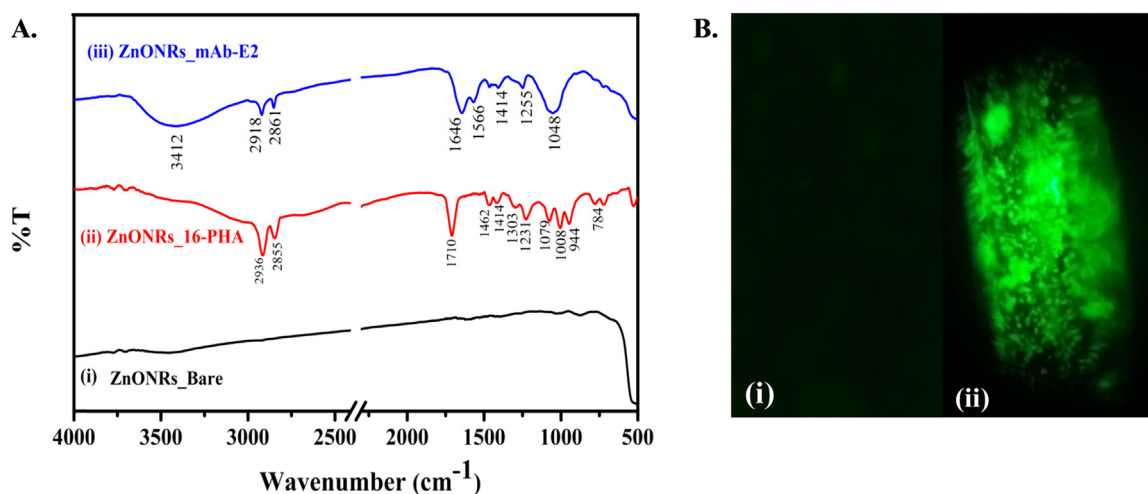
Fig. 1. A. Step wise **s**urface characterization of sensing probe using FTIR in ATR mode at 64 cm^{-1} resolution (i) bare Ag-ZnONRs (ii) 16-PHA functionalized Ag-ZnONRs and (iii) binding of mAb-E2 on Ag-ZnONRs; **B.** Fluorescence microscopic image (i) bare Ag-ZnONRs (ii) 2° FITC labeled antibody bound to Ag-ZnONRs-mAb-E2.

3.1.2. Fluorescence Microscopy studies for mAb-E2 binding on ZnONRs

In order to tune the sensing ability of the electrode surface, the concentration of mAb-E2 need to be optimized. The surface coverage of mAb-E2 coupled to Ag-ZnONRs via 16-PHA was investigated using an inverted fluorescence microscope coupled to a CCD camera. Two different set of electrodes (bare electrode and mAb coupled electrode) were incubated with FITC labeled polyclonal secondary antibody against E2 (pAb-FITC) (1:1000) for 2 h at room temperature. Before excitation, both set of electrodes were thoroughly rinsed with 10 mM PB to remove the unbound fraction of pAb-FITC. The fluorescence imaging was recorded for bare (Fig. 1B (i)) and mAb coupled electrode as shown in Fig. 1B (ii). It is clearly evident from Fig. 1B (ii) that the ZnONRs were sufficiently decorated with mAb-E2. The obtained results indicate effective immobilization of mAb-E2 all over the Ag-ZnONRs electrode surface functionally modified with 16-PHA.

3.1.3. Surface morphological studies using FEG-SEM of Ag-ZnONRs

Further, surface morphology of the Ag-ZnONRs electrode was obtained using FEG-SEM as presented in Fig. 2 (A-C). The micrograph reveals the appearance of high density and highly aligned ZnONRs. Morphological features of ZnONRs covering the Ag surface were studied before and after modification of the ZnONRs. As shown in Fig. 2A (i-iii) ZnONRs grown on the Ag wire substrate have a rod shape, which are primarily aligned horizontally in a flower-like structure. Upon phosphonation, Ag-ZnONRs-16-PHA showed a uniform pattern as depicted in the Fig. 2B. The appearance of phosphorous peak in corresponding EDX spectrum further confirms the phosphonation of Ag-ZnONRs as shown in Supplementary Fig. S1(b). The highly specific antibody mAb-E2 was immobilized onto the 16-PHA-modified Ag-ZnONRs using EDC/NHS coupling chemistry. The appearance of globular structures on the electrode surface strongly confirms that immobilization of the mAb has taken place. The bidentate linkage provided by the actual binding technique ensures efficient surface coverage (Fig. 2C).

3.1.4. Energy-dispersive X-ray spectroscopy (EDX) analysis

The EDX spectra of Ag-ZnONRs electrodes are shown in Supplementary Fig. S1. The peaks corresponding to Zinc element (Zn) and Oxygen (O) can be clearly seen in Fig. S1 (a), which reveals the presence of ZnONRs that contains the elements of Zn and O. Besides that, the signal of Ag attributes to the silver surface itself. In the Fig. S1 (b), the phosphorous (P) and carbon (C) signals were from the 16-PHA used for modifying ZnONRs, for immobilization. The EDX signals were

thus showing that the modification with 16-PHA had been successful. In Fig. S1 (c), EDX signals corresponding to sulphur (S), nitrogen (N) and carbon (C) were recorded, which are characteristic elements, present in the antibody molecule. Therefore, these EDX signals can be used for following and confirming the immobilization of the antibody mAb-E2.

3.1.5. Measurement of sensor surface roughness using AFM

Surface topography is an important parameter that reveals the evidence of nano-structure modification. The surface morphology of bare Ag-ZnONRs, ZnONRs modified with 16-PHA, and Ag-ZnONRs with immobilized mAb-E2 was studied at each step of sensor construction using AFM in semi-contact mode. Various parameters such as average roughness (R_a), root mean square roughness (RMS; R_q) and fractal surface (R_{ku}) value were calculated and analyzed for each step of modification. Fig. 2 (D-F) shows the typical AFM topography of the Ag-ZnONRs coupled electrode before and after modification with 16-PHA and mAb coupling respectively. The average roughness (R_a 1.08 nm) and RMS (R_q 17.09 nm) of 16-PHA modified ZnONRs (Fig. 2E) was decreased over the bare ZnONRs (Fig. 2D) (R_a 42.06 nm and R_q 52.21 nm). The decrease in R_a and R_q parameters of 16-PHA modified ZnONRs indicates the effective phosphonation of the ZnONRs surface. It could be observed that mAb-E2 molecules were immobilized onto the 16-PHA modified Ag-ZnONRs surface as an aggregated pattern keeping its cloud-like structure as in bulk solution as presented in Fig. 2F. It can be further concluded from Fig. 2F that, the coupling of mAb-E2 over the 16-PHA modified Ag-ZnONRs surface was uniform (Ra and Rq values). After immobilization of mAb-E2 on 16-PHA modified ZnONRs surface, the surface roughness (R_a 1.59 nm) and RMS (R_q 39.14 nm) were further increased. On the other hand, the decrease in fractal value of ZnONRs surface from 0.53 to 0.24 strongly suggests the uniform coverage of the mAb immobilization.

3.2. Optimization of sensing parameters

The various assay conditions such as pH, ionic strength, antibody dilutions etc. were optimized as 0.01 M PB, pH 7.4, and mAb dilution 1:1000. The low ionic concentration of 0.01 M PB was used to reduce the effect of charge screening by mobile ions in solution. The mAb-E2 interactions may result into change in conductivity of the insulation layer on the electrodes, charge redistribution and effect on the double layer. The change in capacitance of the immunosensor was recorded for different E2 concentrations in the range 0.01–200 pg mL^{-1}. The capacitance change at low frequency can be attributed to double layer
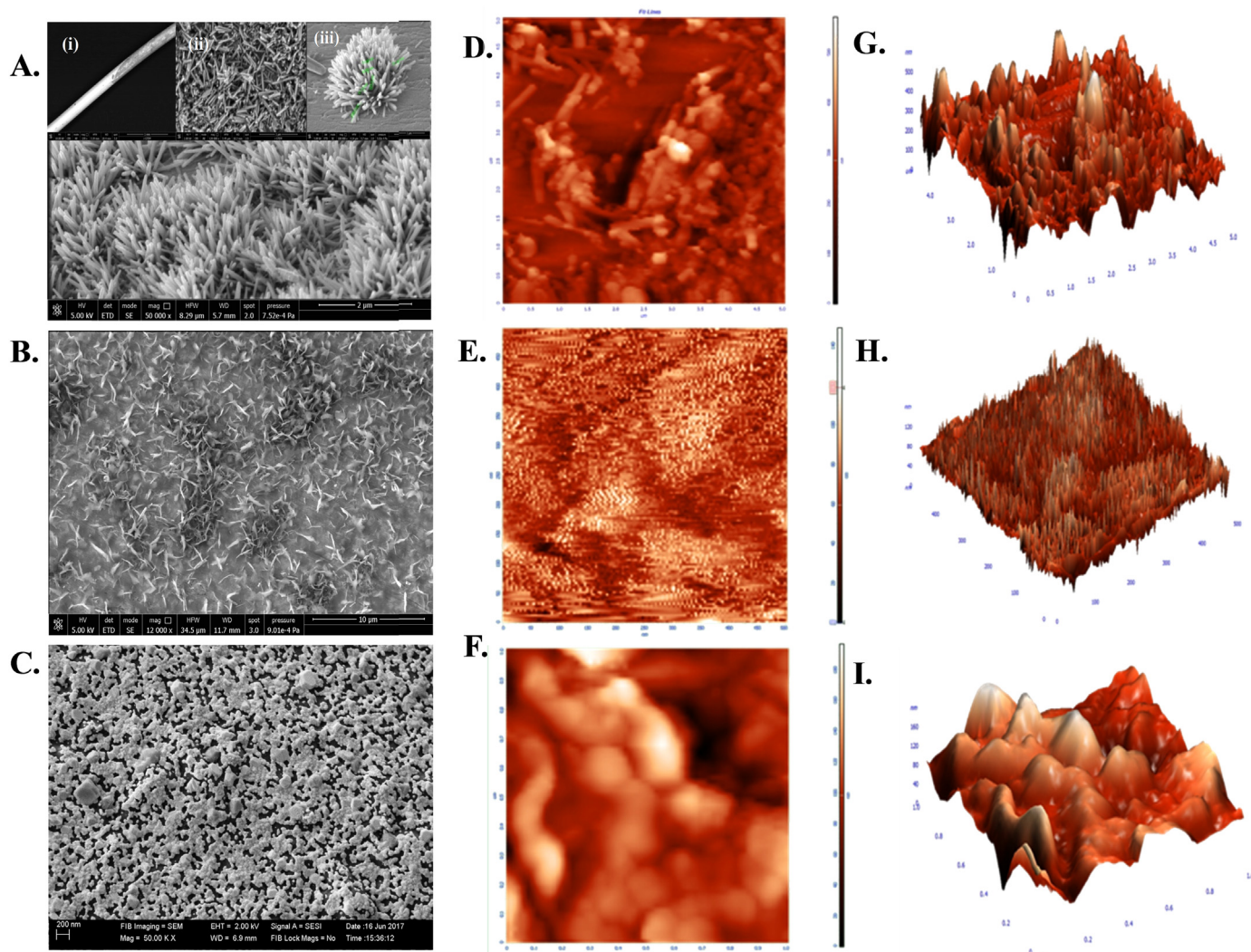
Fig. 2. SEM images of A. Ag-ZnONRs at the magnification of 50,000X with working distance 5.7 mm; Inset **(i)** Ag-ZnONRs electrode at 130X magnification **(ii)** Ag-ZnONRs at 120,000X magnification **(iii)** Flower like structure of ZnONRs at 100,000X magnification B. 16-PHA modified Ag-ZnONRs at 12,000X magnification C. mAb-E2 coupled Ag-ZnONRs at the magnification of 50,000×. AFM surface topography; D. bare Ag-ZnONRs E. 16-PHA modified Ag-ZnONRs electrode F. Ag-ZnONRs-16-PHA-mAb-E2. Height profile using AFM; G. Ag-ZnONRs H. Ag-ZnONRs-16-PHA I. Ag-ZnONRs-16-PHA-mAb-E2.

effects on the electrode surface. A frequency of 1 Hz and applied AC potential 10 mV was selected for analysis, since at this frequency, the significant change in capacitance was observed. The specific interaction of mAb with E2 gave rise to an overall increase in capacitance change from baseline response at the electrode/solution interface.

3.3. Influence of ZnONRs on sensor sensitivity

Herein, we have investigated the immunosensor performance for E2 detection using a bare Ag wire electrode as probe in comparison with an Ag wire with ZnONRs grown onto it. In our previous report, an immunosensor was constructed using a bare Ag wire electrode without ZnONRs and E2 was detectable down to 1 pg mL^{-1} with the same antibody (Singh et al., 2017). However, this sensor was limited by its ability to distinguish E2 concentrations between 0.01 and 0.1 pg mL^{-1}. In this study, the effect of ZnONRs was carried out for lower concentrations of E2. The capacitance response was recorded for the E2 concentration of 0.01 pg mL^{-1} and 0.1 pg mL^{-1} as shown in Fig. 3. Capacitance changes of 13.81% and 18.81% was recorded for the E2 concentration of 0.01 and 0.1 pg mL^{-1} with Ag-ZnONRs-mAb-E2 probe (Figs. 3B and 3D), whereas the capacitance change of only 0.95% and 1.79% was recorded for Ag-mAb-E2 electrode (Figs. 3A and 3C).

3.4. Effect of sample volume on sensor sensitivity and calibration curve

The effect of the assay volume on the sensitivity of the immunosensor was investigated at two different E2 concentrations (1 pg mL^{-1} and 5 pg mL^{-1}) selected from the linear part of the calibration curve. Optimal assay volume is highly important to improve the sensitivity and the lower limit of detection. Therefore, effects of different assay volume from 5 to 90 μL were studied. The impedance response became distorted when measured with sample volumes of 5, 10 and 15 μL due to insufficient coverage of the electrode surface. As shown in the Fig. 4A, the lower assay volume leads to high sensitivity as compare to high assay volume. The working electrode overlapping area was varied for 90 and 20 μL. The improved sensitivity in low sample volume was attributed to directional movement of analyte towards binding site due to enhanced diffusion. However, in case of lower sample volume (20 μL), the electrode surface saturated faster and no further significant change in capacitance was recorded over 90 μL sample volume. Thus, the reaction volume of 90 μL was selected for construction of calibration of sensing curve.

Under optimized experimental conditions, the calibration curve was performed for different E2 concentration spiked in the PB. The capacitive response of Ag-ZnONRs-16-PHA-mAb-E2 immunosensor was
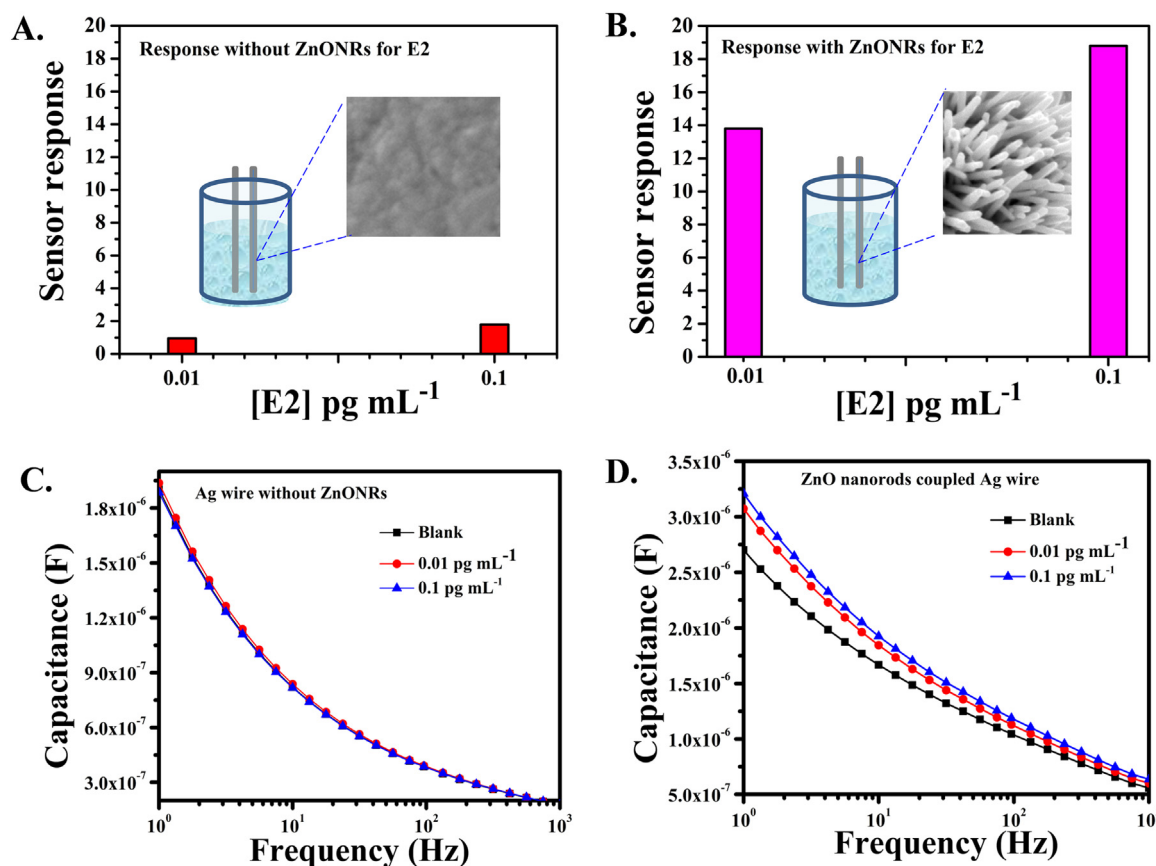
Fig. 3. A. Sensor response of Ag-mAb-E2 B. Sensor response of Ag-ZnONRs-mAb-E2 C. Capacitance spectra of the Ag-mAb-E2 immunosensor D. Capacitance spectra of the Ag-ZnONRs-mAb-E2.

recorded for different E2 concentration ranging 0.1–200 pg mL^{-1} as shown in the Fig. 4B. The % change in capacitance was calculated corresponding to the different concentrations of E2. A dynamic range for E2 detection (0.01–200 pg mL^{-1}) with R^2 = 0.99 and maximum % RSD = 4.35 (n = 3) was obtained and plotted as Fig. 4C. An excellent limit of detection (LOD) 0.01 pg mL^{-1} (S/N = 3) was obtained with a linear range 0.1–200 pg mL^{-1} (inset; Fig. 4C). The limit of quantification (LOQ) was determined with an improved signal to noise ratio 0.1 pg mL^{-1} with the sensitivity of 2.7 % change in capacitance per decade as compared to the other reported methods as summarized in Table 1.

The experimental data obtained from EIS measurement was also validated with the electrical equivalent circuit model as presented in Fig. 4D (inset). The experimental and fitted capacitive spectra of E2 binding is shown Fig. 4D. In the proposed circuit model, constant phase element (CPE) was used over simple capacitor. This is mainly due to surface inhomogeneity, roughness, current and potential distribution of electrode geometry which is raised due to the presence of ZnONRs. The experimental data is fitted with suitable equivalent circuit, which describes the behavior of the capacitive immunosensor. The equivalent circuit mainly consisted of Rs, (R$_{dl}$ CPE$_{dl}$) and (R$_{SAM}$ C$_{SAM}$). The Rs element is interpreted as electrolyte resistance and other two (R$_{dl}$ CPE$_{dl}$) and (R$_{SAM}$ C$_{SAM}$) sub circuit in series attributed for interfacial region. The (R$_{SAM}$ C$_{SAM}$) circuit is attributed to the Gouy-Chapman-Stern layer, resembling a part of SAMs. R$_{SAM}$ is also interpreted as the conductivity (by penetrating ions) of the SAMs. For non-faradic measurement and hence capacitive sensing, R$_{SAM}$ expected to be high to provide insulation. The (R$_{dl}$ CPE$_{dl}$) circuit represents the interaction layer, in which E2 was present. The mAb-E2 layer is represented by constant phase element (CPE) and a parallel resistor R$_{dl}$. It is interesting to note that the CPE phase parameters for SAM and mAb-E2 layer are found to be 0.94 and 0.67. The lower value of phase parameter for

mAb-E2 layer is due to ZnONRs. The validity of the equivalent circuit model is shown as Fig. 4D (inset). The validity is also supported by the fact that its fits the experimental data extremely well for the entire frequency range. The equivalent circuit fitting for each step has been presented in Supplementary Fig. S3, S4 and S5.

3.5. Analytical performance of Ag-ZnONRs immunosensor

The analytical performance of developed immunosensor was verified by inter-electrode and intra-electrode precision performance at a concentration of 1 pg mL^{-1} E2. The inter-electrode precision performance was evaluated with three different electrode prepared independently under similar experimental conditions. The % relative standard deviation (% R.S.D.) value varied in the range 5.08–7.10 for 1 pg mL^{-1} E2, which is a strong indicative of acceptable precision and reproducibility of immunosensor (Table 2). The intra-electrode performance shows a % R.S.D. of 5.01 for three replicate measurements, which proves the practical implementation of developed sensor. The sensitivity of Ag-ZnONRs-16-PHA-mAb-E2 immunosensor was calculated as 2.7% per decade. The presented Ag-ZnONRs-16-PHA-mAb-E2 immunosensor was found to be more sensitive in terms of improved detection limit i.e. 0.01 pg mL^{-1} compare to earlier reported method (0.1 pg mL^{-1}) with further scope of miniaturization.

3.6. Recovery studies from spiked water samples

The practical feasibility of developed ZnONRs based immunosensor was further evaluated in the water sample using standard addition method. After matrix matching, the samples were spiked with various E2 concentration selected from the calibration curve (0.01–200 pg mL^{-1}). Initially, the water samples (Tap and packaged water) were
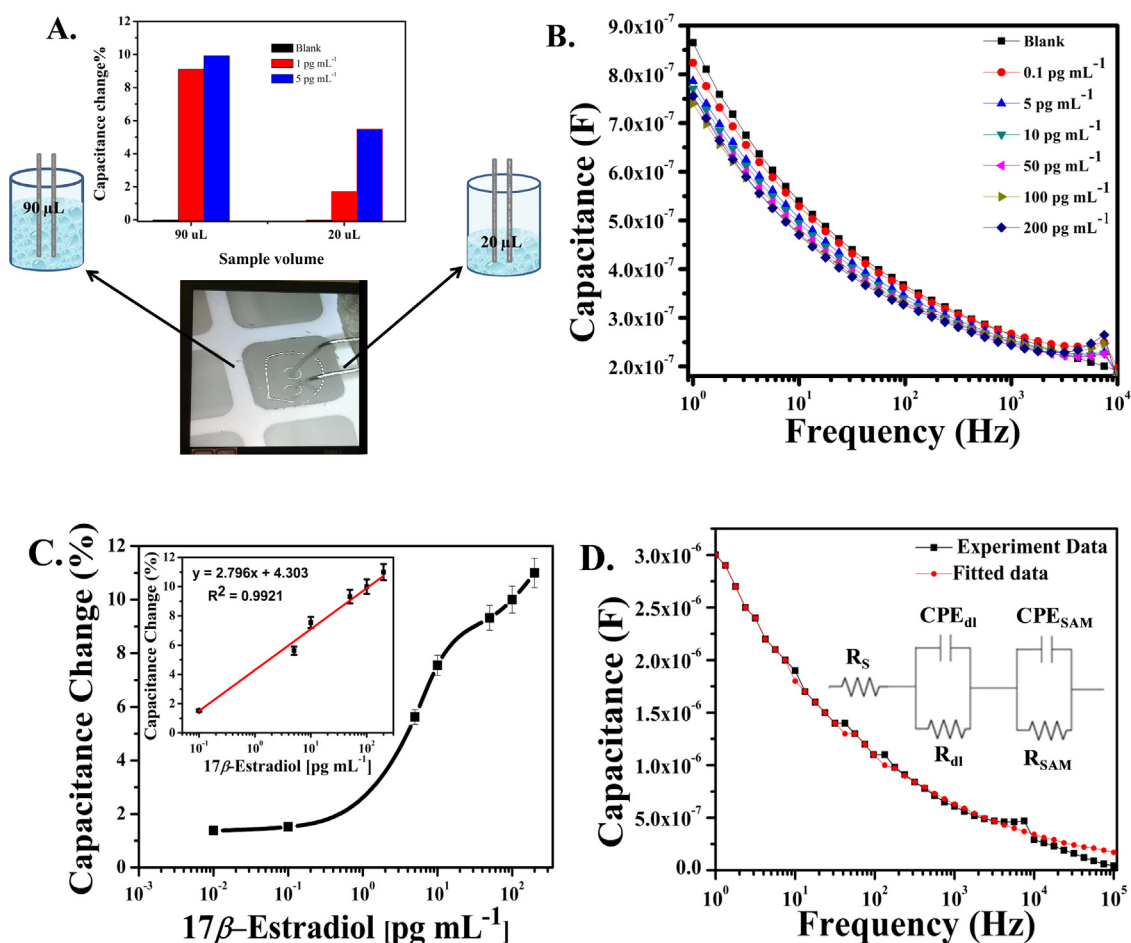
Fig. 4. A. Influence of Ag-ZnONRs-16-PHA-mAb-E2 immunosensor on sample volume investigated for 90 μL and 20 μL against blank, 1 pg mL^{-1} and 5 pg mL^{-1} E2. **B.** Capacitive response of different concentration of E2 (0.1–200 pg mL^{-1}) EIS; 1–100 kHz, AC applied potential of 10 mV **C.** Calibration curve of Ag-ZnONRs-16-PHA-mAb-E2 immunosensor (inset) linear range 0.1–200 pg mL^{-1} R^2 = 0.99 and maximum % RSD = 4.35 (n = 3) with LOD 0.01 pg mL^{-1} **D.** Capacitance spectra in the E2 environment with the fitting curve and (inset) the electrical equivalent circuit.

Table 1
Comparision of literature reported for E2 analysis.

S. No.	Method	Recognition element	LOD	Time	No. of steps	Sensitivity	Reference
1	SWV	Antibody	26 pg mL^{-1}	30 min	6	–	[Liu et al. (2010)]
2	QCM	Antibody	0.04 μg mL^{-1}	60–70 min	5	0.06 μg mL^{-1}	[Chen (2016)]
3	EIS	Estrogen receptor	1.0×10^{-13} M	90 min	5	–	[Kim et al. (2012)]
4	Colorimetric assay	Estrogen receptor	2.62×10^{-14} M	20 min	4	–	[Busayapongchai and Siri (2017)]
5	EIS	Antibody and Estrogen receptor	500 p.M.	21 min	5	–	[Furst et al. (2017)]
6	ELISA	Antibody	1.48 pg mL^{-1}	95 min	4	1.48% (Indirect method); 1.81% (Direct method)	[Xin et al. (2010)]
7	Optical assay (Fluorescence)	Aptamer	6.37×10^{-6} ng mL^{-1}	180 min	5	–	[Du et al. (2015)]
8	EIS	Antibody	1 pg mL^{-1}	10 min	3	1.4%	[Singh et al. (2017)]
9	SPR	Antibody	10^{-3} ng mL^{-1}	40 min	4	–	[Boltovets et al. (2017)]
10	**EIS; ZnO nanorods based**	**Antibody**	**0.01 pg mL^{-1}**	**10 min**	**3**	**2.7%**	**This work**

assumed to be E2 free. The recoveries performance of Ag-ZnONRs-16-PHA-mAb-E2 immunosensor were found between 97.5% and 109% with % RSD 2.72–3.26 (n = 4) for 1, 10 and 50 pg mL^{-1} concentration as presented in Supplementary table (ST1). The obtained results suggested that the developed method was in good agreement in terms of sensitivity, reproducibility for E2 detection and showed practical utility. Out of the two samples one sample was found to be positive.

4. Conclusions

In the present work, a novel nanostructure (ZnONRs) integrated ultrasensitive Ag-ZnONRs-16-PHA-mAb-E2 immunosensor for detection of E2 in water with LOD 10 femtogram (0.01 pg mL^{-1}) is demonstrated. The integration of ZnONRs to sensing electrode enabled higher sensitivity over earlier reported work without ZnONRs. A linear range 0.1–200 pg mL^{-1} for E2 detection was achieved with significant

Table 2

Analytical precision peformance of developed immunosensor for E2 detetcion.

Inter-electrode response					
E2 [pg mL^{-1}]	Capacitance change %			Mean ± S.D.	%RSD
1	9.92	9.65	8.98	9.517 ± 0.484	5.08
1	8.65	9.91	9.04	9.200 ± 0.645	7.01
1	10.52	9.24	9.428	9.729 ± 0.691	7. 10
Intra-electrode response					
E2 [pg mL^{-1}]	Capacitance change%			Mean ± S.D.	%RSD
1	9.92	8.98	9.58	9.493 ± 0.475	5.01

enhancement in the sensitivity at 2.7% capacitance change per decade. The limit of quantification is achieved down to 0.1 pg mL^{-1}. A further increase in sensitivity was achieved by way of assay volume reduction thus enabling further scope for miniaturization. A good intra-electrode precision performance with % R.S.D. of 5.01 (n = 3) was recorded. This approach could be potentially expanded to an array-based technology for EDCs sensing.

Acknowledgment

Conflict of interest

Authors declare no conflicts of interest.

Appendix A. Supporting information

Supplementary data associated with this article can be found in the online version at doi:10.1016/j.bios.2018.10.004.

References

Ahmad, M., Pan, C., Iqbal, J., Gan, L., Zhu, J., 2009. Chem. Phys. Lett. 480 (1), 105–109.
Ahmad, M., Pan, C., Luo, Z., Zhu, J., 2010. J. Phys. Chem. C 114 (20), 9308–9313.
Asif, M.H., Fulati, A., Nur, O., Willander, M., Brännmark, C., Strålfors, P., Börjesson, S.I., Elinder, F., 2009. Appl. Phys. Lett. 95 (2), 023703.
Asif, M.H., Ali, S.M.U., Nur, O., Willander, M., Brännmark, C., Strålfors, P., Englund, U.H., Elinder, F., Danielsson, B., 2010a. Biosens. Bioelectron. 25 (10), 2205–2211.
Asif, M.H., Nur, O., Willander, M., Strålfors, P., Brännmark, C., et al., 2010b. Materials 3, 4657–4667.
Boltovets, P., Shinkaruk, S., Vellutini, L., Snopok, B., 2017. Biosens. Bioelectron. 90, 91–95.
Bülbül, G., Hayat, A., Andreescu, S., 2015. Sensors 15 (12), 29826.
Bulusu, A., Paniagua, S.A., MacLeod, B.A., Sigdel, A.K., Berry, J.J., Olson, D.C., Marder, S.R., Graham, S., 2013. Langmuir 29 (12), 3935–3942.
Busayapongchai, P., Siri, S., 2017. Anal. Biochem. 518, 60–68.
Chen, D., 2016. Int. J. Environ. Anal. Chem. 96 (14) (1389-1401-2016 v.1396 no.1314).
Codex Alimentarius Commission, 2012. CAC/MRL 2–2012, 1–40.
Cornil, D., Van Regemorter, T., Beljonne, D., Cornil, J., 2014. Phys. Chem. Chem. Phys. 16 (38), 20887–20899.
Damstra, T., Barlow, S., Bergman, A., Kavlock, R.J., Van Der Kraak, G. (Eds.), 2002. World Health Organization.
Du, L., Ji, W., Zhang, Y., Zhang, C., Liu, G., Wang, S., 2015. Analyst 140 (6), 2001–2007.
Furst, A.L., Hoepker, A.C., Francis, M.B., 2017. ACS Cent. Sci. 3 (2), 110–116.
Hsuan, K., Andrew, T., 2015. J. Phys. Condens. Matter 27 (5), 054007.
Kim, B.K., Li, J., Im, J.-E., Ahn, K.-S., Park, T.S., Cho, S.I., Kim, Y.-R., Lee, W.-Y., 2012. J. Electroanal. Chem. 671, 106–111.
Le, N.D.B., Wang, X., Geng, Y., Tang, R., Tonga, G.Y., Jiang, Z., Rotello, V.M., 2017. Chem. Commun. 53 (62), 8794–8797.
Liu, X., Duckworth, P.A., Wong, D.K.Y., 2010. Biosens. Bioelectron. 25 (6), 1467–1473.
Luo, X., Morrin, A., Killard, A.J., Smyth, M.R., 2006. Electroanalysis 18 (4), 319–326.
Nohynek, G.J., Borgert, C.J., Dietrich, D., Rozman, K.K., 2013. Toxicol. Lett. 223 (3), 295–305.
Pal, S., Bhand, S., 2015. Microchim. Acta 182 (9), 1643–1651.
Perumal, V., Hashim, U., Gopinath, S.C.B., Haarindraprasad, R., Foo, K.L., Balakrishnan, S.R., Poopalan, P., 2015. Sci. Rep. 5, 12231.
Rosner, W., Hankinson, S.E., Sluss, P.M., Vesper, H.W., Wierman, M.E., 2013. J. Clin. Endocrinol. Metab. 98 (4), 1376–1387.
Singh, A.C., Bacher, G., Bhand, S., 2017. Electrochim. Acta 232, 30–37.
Soleymani, L., Fang, Z., Sargent, E.H., Kelley, S.O., 2009. Nat. Nanotechnol. 4, 844.
Sonnenschein, C., Soto, A.M., 1998. J. Steroid Biochem. Mol. Biol. 65 (1), 143–150.
Soomro, M.Y., Hussain, I., Bano, N., Nur, O., Willander, M., 2012. Phys. Status Solidi (RRL) – Rapid Res. Lett. 6 (2), 80–82.
Viter, R., Savchuk, M., Iatsunskyi, I., Pietralik, Z., Starodub, N., Shpyrka, N., Ramanaviciene, A., Ramanavicius, A., 2018. Biosens. Bioelectron. 99, 237–243.
Wang, J., 2005. Small 1 (11), 1036–1043.
Willander, M., Klason, P., Yang, L.L., Al-Hilli, S.M., Zhao, Q.X., Nur, O., 2008. Phys. Status Solidi C 5 (9), 3076–3083.
Xia, C., Wang, N., Wang, L., Guo, L., 2010. Sens. Actuators B 147 (2), 629–634.
Xin, T.-B., Chen, H., Lin, Z., Liang, S.-X., Lin, J.-M., 2010. Talanta 82 (4), 1472–1477.
Yakimova, R., Selegard, L., Khranovskyy, V., Pearce, R., Spetz, A.L., Uvdal, K., 2012. Front. Biosci. 254–278.
Yue, H.Y., Huang, S., Chang, J., Heo, C., Yao, F., Adhikari, S., Gunes, F., Liu, L.C., Lee, T.H., Oh, E.S., Li, B., Zhang, J.J., Huy, T.Q., Luan, N.V., Lee, Y.H., 2014. ACS Nano 8 (2), 1639–1646.
Zhu, C., Yang, G., Li, H., Du, D., Lin, Y., 2015. Anal. Chem. 87 (1), 230–249.
Zoeller, R.T., Brown, T.R., Doan, L.L., Gore, A.C., Skakkebaek, N.E., Soto, A.M., Woodruff, T.J., Vom Saal, F.S., 2012. Endocrinology 153 (9), 4097–4110.